

CAN HIGH-RESOLUTION MOISTURE FIELDS BE RETRIEVED IN SUPERCELLS?

D. Bodine^{1,2,*}, R. D. Palmer^{1,2}, B. L. Cheong², P. L. Heinselman³, D. S. Michaud^{1,2}, and G. Zhang^{1,2}

¹ School of Meteorology, The University of Oklahoma, Norman, OK, U.S.A.

² Atmospheric Radar Research Center, The University of Oklahoma, Norman, OK, U.S.A

³ NOAA/OAR National Severe Storms Laboratory, Norman, OK, U.S.A

1. INTRODUCTION

The thermodynamic characteristics of the rear flank downdraft (RFD) and ambient environment have important implications on tornadogenesis. Moist surface conditions produce lower lifted condensation levels (LCLs), which are more favorable for significant tornadoes (Rasmussen and Blanchard, 1998). In a study of 30 supercell cases, Markowski et al. (2002) found that high-boundary layer relative humidities produce more buoyant RFDs and increase the likelihood of tornadogenesis. Markowski et al. (2002) also found that smaller differences in equivalent potential temperature, θ_e , and virtual potential temperature, θ_v , between the RFD and the environment increased the likelihood of tornadogenesis and the intensity and duration of the tornadoes. The warm RFDs (smaller difference in θ_e) produce stronger tornadoes than cool RFDs (larger difference in θ_e) because the warm RFDs have greater buoyancy and increase low-level convergence. These observational findings were later confirmed by modeling studies, which also showed that high-boundary layer humidities and small θ_e differences were favorable for tornadogenesis (Markowski et al., 2003). Markowski and Richardson (2009) suggested that boundary layer humidity is one of the most promising variables for forecasters to distinguish tornadic and nontornadic supercells.

Markowski et al. (2002) speculated that high-resolution, near-surface thermodynamic measurements are one of the most critical measurements for improving scientific understanding of tornadogenesis. Radar refractivity measurements (Fabry et al., 1997; Fabry, 2004; Cheong et al., 2008) could partially address this issue by providing surface moisture measurements in supercell environments with up to 4-km spatial resolution. Recent studies have shown that refractivity data can reveal moisture changes associated with drylines, boundary layer processes, convection initiation, outflow boundaries, mesocyclones, and others (Weckwerth et al., 2005; Fabry, 2006; Demoz et al., 2006; Buban et al., 2007; Roberts et al., 2008; Wakimoto and Murphey, 2008; Bodine et al., 2008, 2009a,b; Heinselman et al., 2009).

This paper will develop the theory of refractivity errors caused by precipitation, and present case studies illustrating

the capability to use refractivity data for supercell and tornadogenesis observations and forecasting. The radar refractivity retrieval algorithm will be described in Section 2, and the theory of refractivity errors caused by precipitation will be developed in Section 3. Section 4 presents two supercell case studies from 8 April 2008 and 1 May 2008.

2. RADAR REFRACTIVITY RETRIEVAL ALGORITHM

The ARRC has developed an independent algorithm for refractivity retrieval based on the work by Fabry et al. (1997). The University of Oklahoma algorithm has been adapted easily for different weather radars, including the Weather Surveillance Radar-1988 Dopplers (WSR-88Ds), the Collaborative Adaptive Sensing of the Atmosphere (CASA; McLaughlin et al., 2009) X-Band Radars, and the National Weather Radar Testbed (NWRT) Phased Array Radar (PAR; Zrnić et al., 2007), for example. Cheong et al. (2008) provide a detailed description of the University of Oklahoma refractivity algorithm, although it is briefly described here for completeness.

The refractive index, n , is often rewritten in terms of refractivity, N , to improve the ease of interpretation (Bean and Dutton, 1968);

$$N = (n - 1) \times 10^6. \quad (1)$$

Bean and Dutton (1968) showed that refractivity could be related to temperature, pressure and water vapor pressure using the following equation,

$$N = 77.6 \frac{p}{T} + 3.73 \times 10^5 \frac{e}{T^2}, \quad (2)$$

where p is pressure in millibars, T is the temperature in Kelvin, and e is the water vapor pressure in millibars. At warmer temperatures, refractivity provides a good approximation for surface moisture, as temperature and pressure changes affect refractivity less than moisture changes.

Radar refractivity retrievals are obtained using phase measurements between the radar and ground clutter targets. Reference phase measurements are made when the moisture field is nearly homogeneous and constant with time. At the same time, an objectively analyzed refractivity field is derived from Oklahoma Mesonet (Mesonet, hereafter) data (Brock et al., 1995; McPherson et al., 2007) to create a

* Corresponding author address: David Bodine, University of Oklahoma, School of Meteorology, 120 David L. Boren Blvd., Rm 4630, Norman, OK 73072-7307; e-mail: bodine@ou.edu

reference refractivity field. Real-time phase measurements are collected to produce a phase difference field using the reference and real-time phase measurements. Poor clutter targets are then censored based on clutter quality indices. The resulting phase difference field is relatively noisy and sparse, so the phase difference field is smoothed using a 2.5-km Gaussian window. Next, the radial derivative of the phase difference field is computed to obtain the refractivity change field. The resulting refractivity change field is subsequently smoothed to reduce the noise introduced by the derivative operation. Absolute refractivity (hereafter, refractivity) can be computed by adding the refractivity change and the reference refractivity fields. Scan-to-scan refractivity change (hereafter, scan-to-scan refractivity) is computed by substituting the phase measurements from the previous scan for the reference phase measurements, and applying the same procedure to the phase difference data.

3. PRECIPITATION EFFECTS THEORY AND MITIGATION

3.1. Phase Variance Contribution by Precipitation

The phase data obtained for refractivity measurements can be analyzed directly from the time series signal using a Discrete Fourier Transform. When precipitation and clutter targets are present in the range gate, the incident energy is backscattered by both targets. Hence, both targets contribute to the phase measurement used in refractivity retrievals. Because the refractivity algorithm is not intended to use phase measurements from precipitation, removing the phase contribution from precipitation could improve radar refractivity retrievals in regions with precipitation. The QI may remove regions with precipitation where the signal is dominated by precipitation, thus reducing the areal coverage of refractivity measurements. Figure 1 illustrates the absence of refractivity retrievals in regions with heavy precipitation where phase data were censored. The scan-to-scan refractivity data are also noisy, indicating poor quality of phase measurements throughout the field. This section will describe a method of filtering the precipitation signal to improve the ground clutter signal, which could result in better refractivity coverage and more accurate refractivity measurements in regions with precipitation.

The combination of ground clutter and weather signals is clearly observed in both the time and frequency domains. Figure 2 shows the in-phase, and quadrature signals, and the amplitude and phase after taking the DFT for a combination of clutter and weather signals. Two peaks are observed in the Doppler spectrum, indicating stationary target(s) and moving target(s). Both targets exhibit a high SNR, so the signal is likely a combination of ground clutter and precipitation.

Filters can be designed to mitigate undesired signals. Ground clutter filters are typically high-pass filters that attenuate the ground clutter signal at near-zero frequency, and preserve the weather signal at higher frequencies (e.g., Torres and Zrnić, 1999). Similarly, a low-pass filter could be implemented to attenuate the weather signal (higher frequency content), and simultaneously preserve the ground clutter signal. Hence, a low-pass filter could improve the phase measurements in regions of precipitation.

The OU Refractivity algorithm currently averages the I and Q data before computing the phase. The averaging is effectively a low-pass filter with equal filter coefficients. This “averaging” filter produces relatively high sidelobes (Fig. 3a), but a narrow pass band (Fig. 3b). When the filter length is extended, the width of the pass band decreases and the magnitude of the sidelobes decrease. The number of pulses averaged by the OU algorithm depends on the VCP. In clear-air modes, the number of pulses ranges from 60 to 80, whereas in precipitation modes the number of pulses is only 15 to 20. Given the high sidelobes when integrating fewer pulses (precipitation mode), all of the precipitation signal may not be attenuated, particularly for heavy, or slowly moving precipitation. Hence, for refractivity retrievals in areas with heavier precipitation, decreased sidelobes are needed to further attenuate the precipitation signal.

To address this problem, a filter with lower sidelobes was designed. Fig. 4 shows several window functions that were considered for the design of the low-pass filter. The primary tradeoff is between the width of the pass band and the sidelobe levels. The rectangular window generates a narrow pass band and high sidelobes, whereas the hamming window generates a wider pass band and a much lower sidelobes. The Hamming and triangular windows present a compromise between the two tradeoffs. However, the difference in pass band width is relatively small among the Hanning, Hamming, and triangular windows, while the differences in sidelobe levels are much greater. Based on the frequency response of the four windows, the low sidelobe levels of the Hanning window will provide better attenuation of precipitation, and the pass band width of the Hanning window is close to the Hamming and triangular window. Thus, a filter design based on a Hanning window should produce the best filtered signal for refractivity processing.

The filter implemented on the I and Q data for refractivity processing (hereafter weather clutter filter, or WC filter) was based on the Hanning window. The filter produces a linear phase shift, which must be corrected for accurate phase measurements. For a zero-phase filter, the data are filtered forward and then in reverse, resulting in zero-phase shift and doubled the filter order. Increasing the length of the WC filter resulted in a more narrow pass band, and reduced sidelobe levels (Fig. 5). The WC filter will perform optimally in regions of fast-moving precipitation because the WC filter attenuates higher frequencies. In regions of slow-moving precipitation,

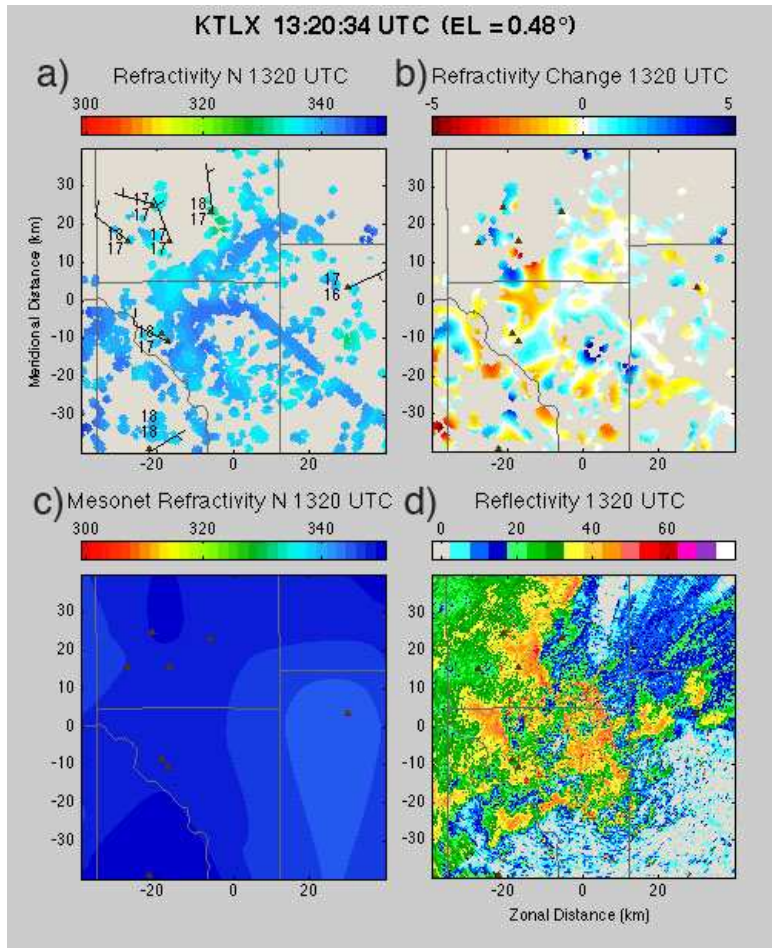


Figure 1: a) Refractivity, b) scan-to-scan refractivity, c) Mesonet refractivity, and d) reflectivity at 1320 UTC 8 May 2007. Regions of the refractivity field are missing because the censoring process removed areas of precipitation.

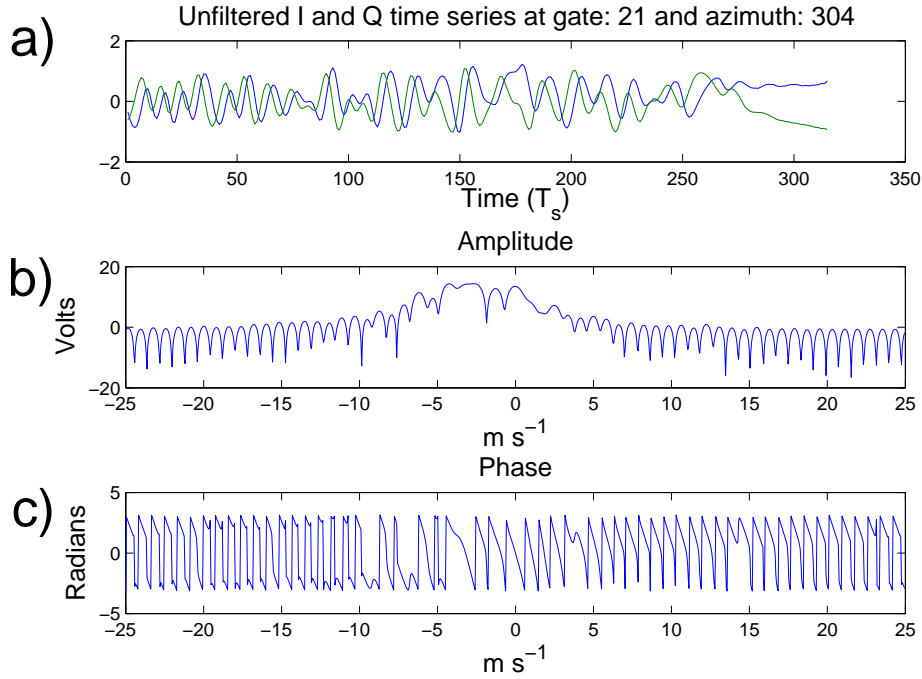


Figure 2: This figure shows an example of I and Q data, and the resulting amplitude and phase data after the DFT for a combination of ground clutter and weather signals. The a) in-phase (blue) and quadrature (green) signals are used to compute the DFT, yielding the b) amplitude and c) the phase over a distribution of velocities (x-axis). The peak amplitude occurs at two distinct peaks (approximately 0 m s^{-1} and -4 m s^{-1}). Hence, the DFT shows that the target is likely a combination of ground clutter and weather signals.

or where the radial velocity is small but the precipitation has a large velocity in the azimuthal direction, the WC filter will not significantly attenuate the weather signal, and the “averaging” filter remains a better choice because of the very narrow pass band.

To study the impact of the WC filter on phase, Level-I data from KTLX was obtained for 7–8 May 2008 during a period of persistent rainfall. A 5-hour period of Level-I data between 2047 UTC 7 May and 0156 UTC 8 May 2008 was analyzed. The Level-I data were binned into 1° azimuth angles for processing, and the in-phase and quadrature signals were filtered using the WC filter. To avoid undesired windowing effects, the length of the data window was increased by filtering over three azimuth angles to increase the number of pulses. Then, the data window was truncated by 1° azimuth angle after filtering. The phase was calculated using

$$\phi = \tan^{-1} \left(\frac{\overline{Q(t)}}{\overline{I(t)}} \right), \quad (3)$$

where ϕ is the phase, $\overline{I(t)}$ and $\overline{Q(t)}$ are the mean in-phase and quadrature signals. The phase was computed for the unfiltered and filtered in-phase and quadrature signals.

To develop thresholds for good and bad clutter points, a bad clutter point was defined as a range gate below a real-time RI threshold. Normally, the RI is only computed when the moisture field is almost spatially homogeneous and temporally invariant. However, the real-time RI can still be used because good clutter targets should exhibit greater phase coherence with time compared to poor clutter targets. The real-time RI was computed for a data set of 16100 points (gates 5–50, all azimuth angles). The RI improvement was defined as the difference between the unfiltered and filtered real-time RI. Fig. 6a shows that the mean improvement after filtering is greatest for low real-time RI, especially during the period of heavier precipitation (Fig 6b). The number of good targets decreased significantly as the real-time RI threshold was increased (Fig. 7a). The mean RI improvement was greatest when the real-time RI threshold was set to 0.5 (Fig. 7b), resulting in a mean RI improvement of 0.2 (excluding gates where RI improvement

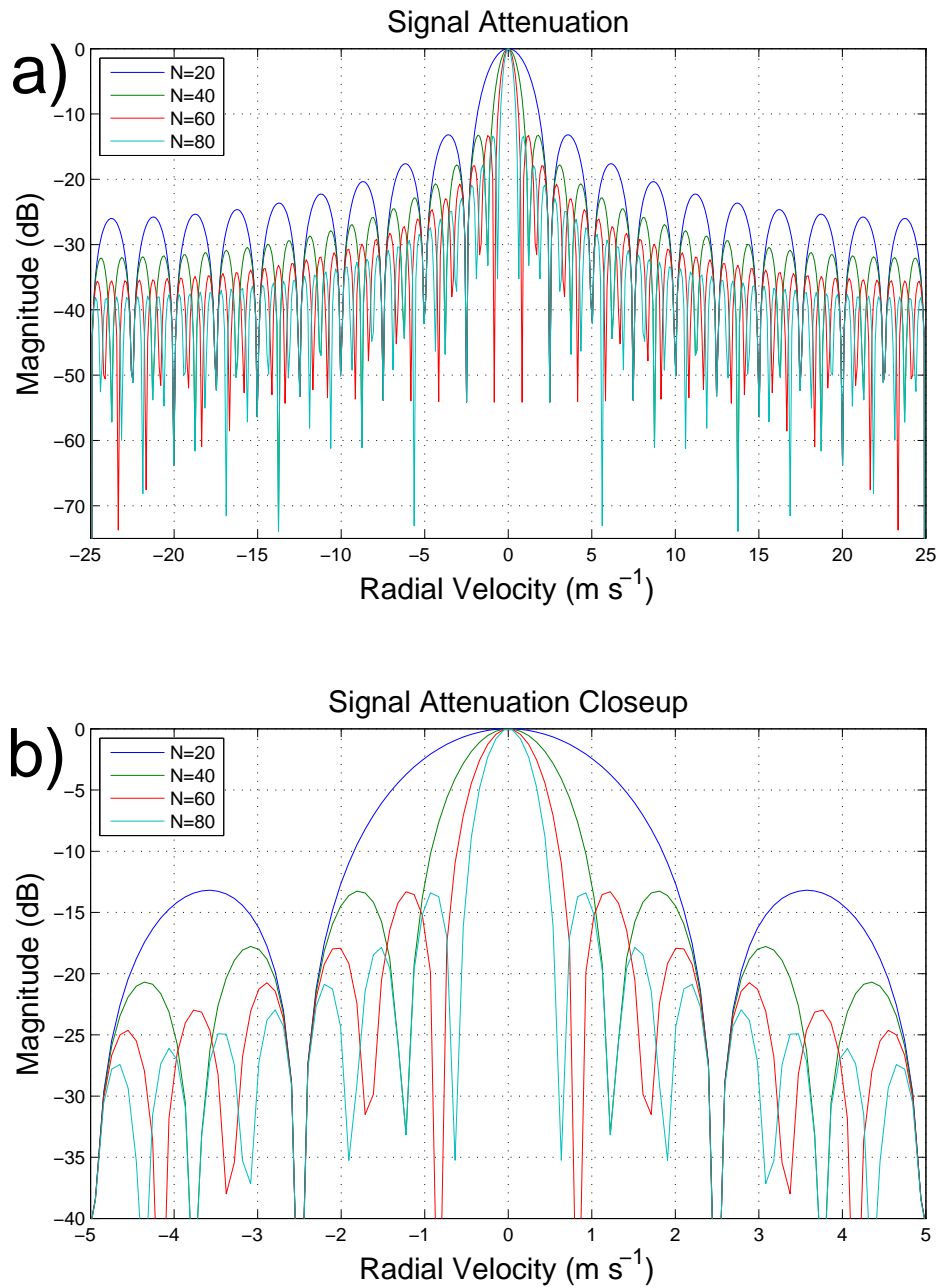


Figure 3: a) Signal attenuation of the “averaging” filter for 20, 40, 60, and 80 pulses, and b) close-up of signal attenuation in the pass band. The filter produces a narrow pass band between $\pm 2.5 \text{ m s}^{-1}$ at 20 pulses and $\pm 0.7 \text{ m s}^{-1}$ at 80 pulses. However, the magnitude of the sidelobes is relatively high.

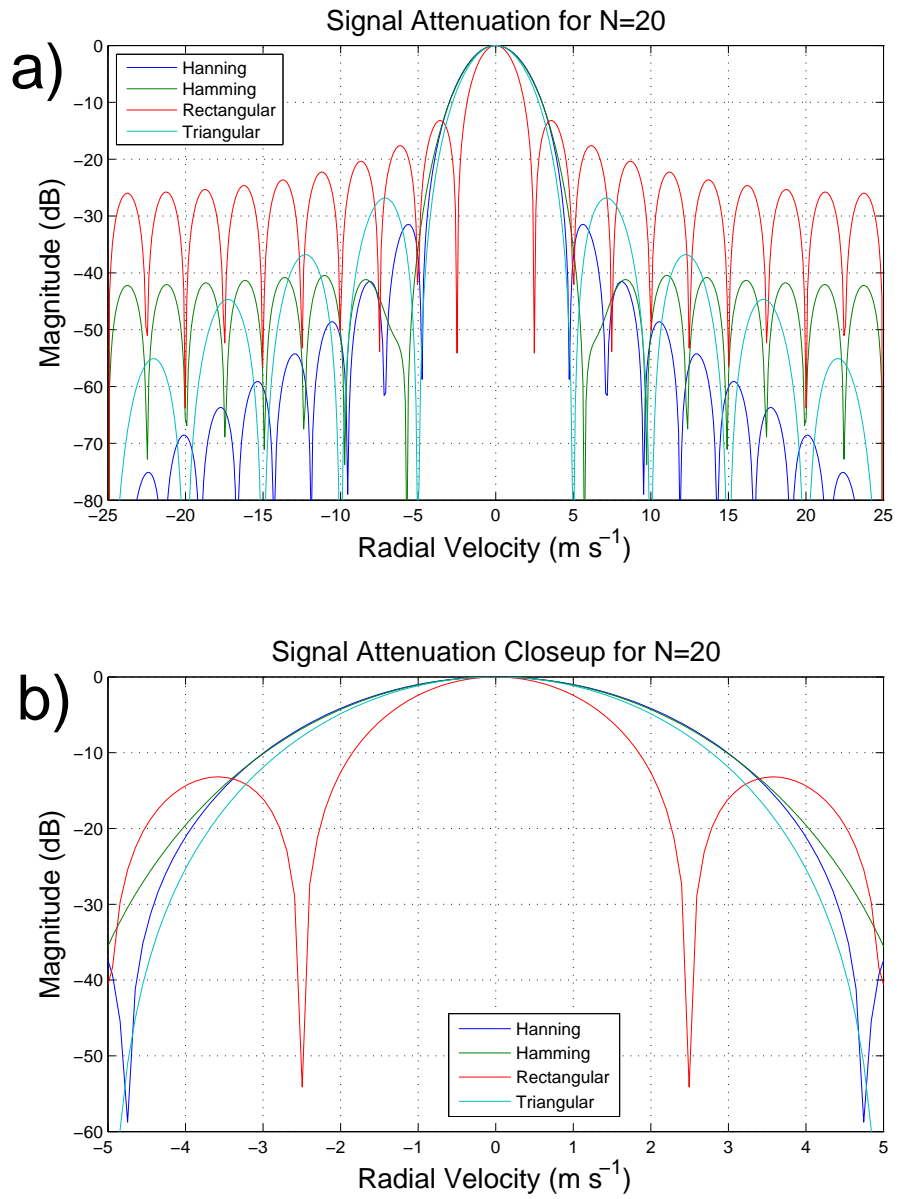


Figure 4: a) Plot of signal attenuation using 20-tap rectangular, triangular, Hamming, and Hanning windows, and b) close-up of the signal attenuation in the pass band. The Hanning window generates the largest stop band attenuation, while the rectangular window generates the most narrow pass band.

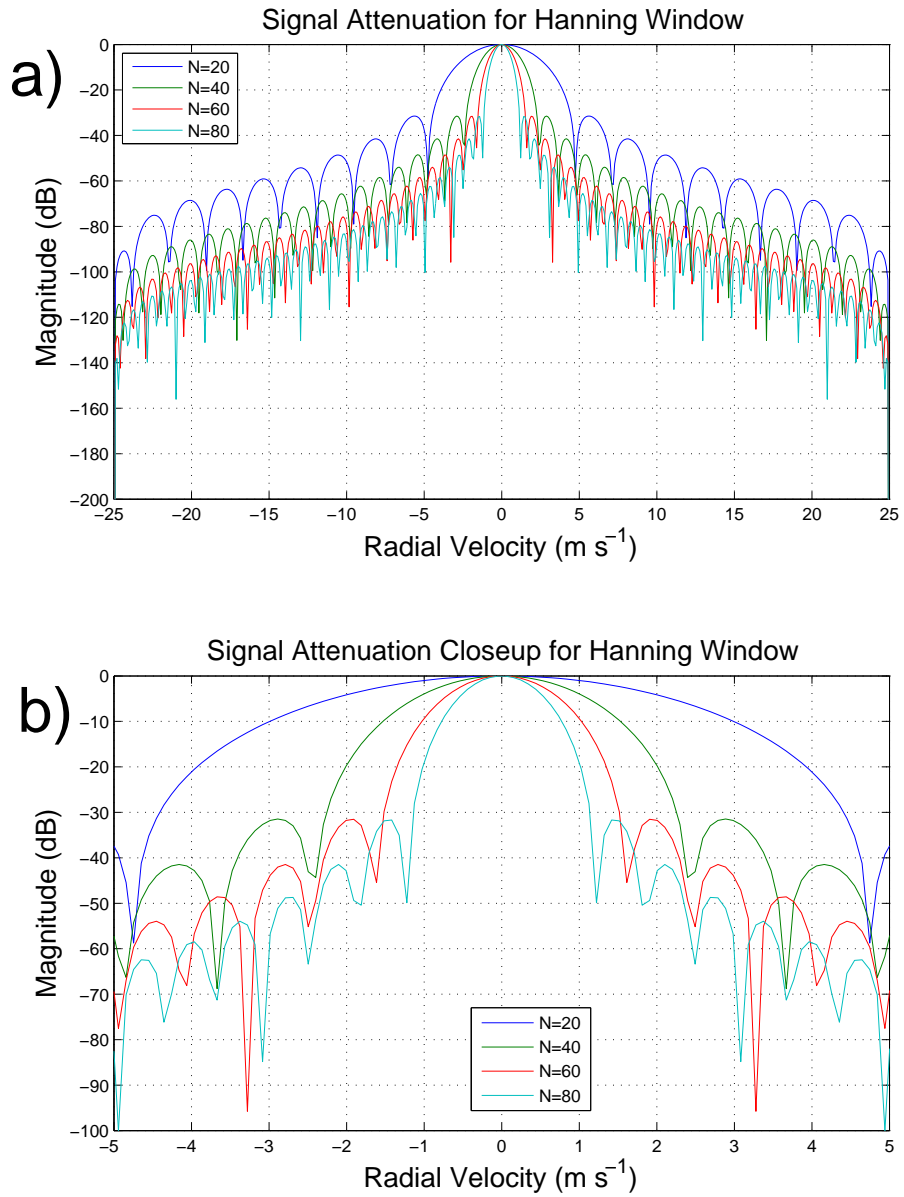


Figure 5: a) Plot of signal attenuation using 20, 40, 60, and 80-tap Hanning windows, and b) close-up of the signal attenuation in the pass band. The higher-order filters produce a narrower pass band and lower sidelobe levels.

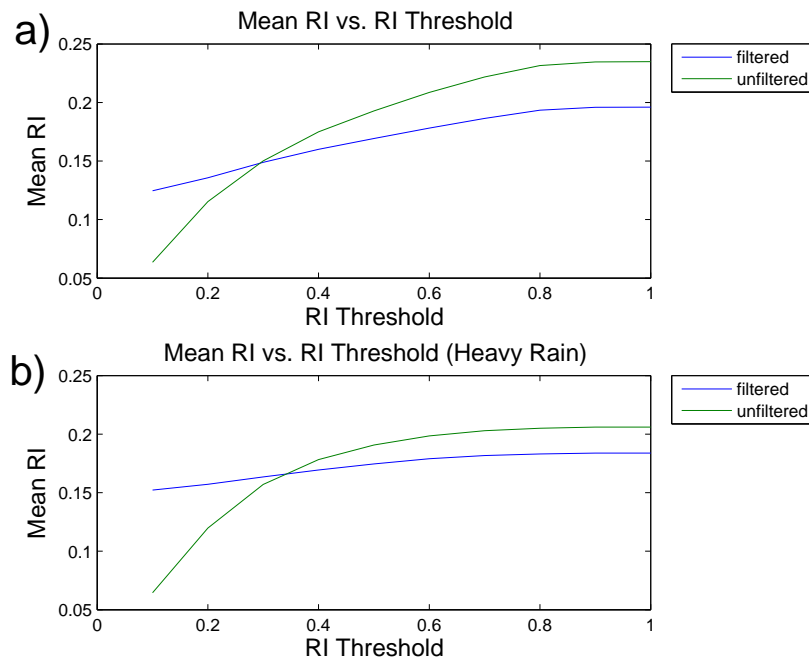


Figure 6: a) Plot of the mean RI for all range gates up to the real-time RI threshold (x-axis), b) same as a) except for period of heavy rainfall. The mean real-time RI for the filtered, and unfiltered approximated phase is shown. For poor targets (low RI), the WC filter significantly improved the mean RI. For good targets (high RI), the WC filter decreased the mean RI compared to the unfiltered mean RI.

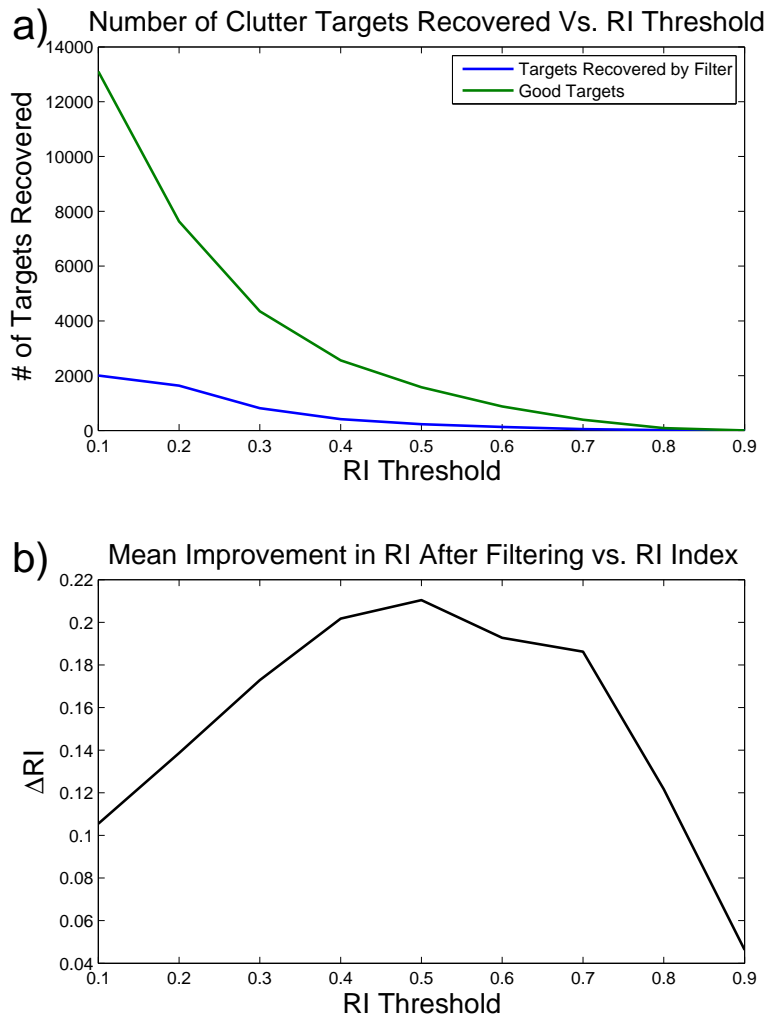


Figure 7: Plots showing a) number of clutter targets recovered given a set real-time RI threshold, and b) mean improvement in RI after filtering for a set real-time RI threshold. The largest improvement occurs for a real-time RI threshold of 0.5.

was negative). A surprising result was that the mean RI for good clutter targets decreased after filtering (Fig. 6a), as the mean RI decreased when the real-time RI threshold was above 0.5. This counter-intuitive result could be explained by the wider pass-band allowing greater signal contamination at lower frequencies within the intersection of the stop band of the “averaging filter” and the pass band of the WC filter.

A time-series of unfiltered and filtered phase was also produced for different filter orders. High-order filters narrow the width of the pass band and reduce sidelobes. However, the wider data window may have the undesired effect of allowing weather or poor clutter targets within the data window. Hence, using a high-order filter does not necessarily improve performance. The RI over the 5-hour period was computed for different filter orders over the full study period and over the first two hours when heavy precipitation covered most of the gates within the domain. As the filter order increased from 20 to 80, the mean RI remained nearly constant.

Given the poor performance of the filter for clutter targets with high RI, an adaptive filter could be designed and applied to only poor clutter targets (below RI threshold). Furthermore, the RI improvement could also be computed, and used to determine if the unfiltered or filtered phase is selected for refractivity processing. To implement the WC filter for refractivity, the real-time RI would be needed and thresholds should be established to determine which range gates should be filtered. The WC filter could be implemented relatively easily into the refractivity algorithm. The WC filter is a time-domain filter, so the primary operation is a convolution, which can be computationally efficient. An example of a potential application of radar refractivity retrievals in supercells will be discussed in Section 4, illustrating an application within regions of heavy precipitation.

3.2. Precipitation Bias

Refractivity bias occurs in precipitation because the radar-measured refractivity is not only caused by the atmosphere, but has contributions from the precipitation. The precipitation causes additional propagation delay, caused by increased refractive index resulting in a positive bias. These effects are undesirable, as the goal of refractivity retrievals is to provide a radar-based estimate of atmospheric moisture. This section provides a background on the precipitation bias, a method of estimating the bias, and suggestions for mitigation.

The change in refractivity is proportional to the radial gradient in phase difference between time t_1 and t_0 . The change in phase difference, $\Delta\phi$, can be written in two components,

$$\Delta\phi = \Delta\phi_{air} + \Delta\phi_{rain}, \quad (4)$$

where $\Delta\phi_{air}$ is the phase change caused by air, and $\Delta\phi_{rain}$ is the phase change caused by precipitation. The total change in refractive index, Δn , can then be written as

$$\Delta n = \Delta n_{air} + \Delta n_{rain}, \quad (5)$$

where Δn_{air} is the refractive index change caused by air, and Δn_{rain} is the refractive index change caused by precipitation. Assuming there is no precipitation at time t_0 (reference scan), there is no contribution of precipitation to phase ($\phi_{rain}(r, t_1) = 0$), so the phase change caused by precipitation can be written as $\Delta\phi_{rain} = \phi_{rain}(r, t_1)$. The change in refractive index caused by rain can be written as

$$\Delta n_{rain} = n_{mix} - n_{air}, \quad (6)$$

where n_{mix} is the refractive index of the mixture of air and precipitation, n_{air} is the refractive index of air, and Δn_{rain} is the change in refractive index caused by rain. (6) can be converted into refractivity using (1).

The Maxwell-Garnet mixing formula can compute the refractive index of the air/water mixture, assuming water as the enclosure and a known drop-size distribution (DSD). The polarizability, y , can be calculated using

$$y = \frac{\epsilon_{water} - \epsilon_{air}}{\epsilon_{water} + 2\epsilon_{air}}, \quad (7)$$

where ϵ_{water} is the dielectric constant of water, and ϵ_{air} is the dielectric constant of air. The fractional volume of water, f_w , is proportional to the third-moment of the DSD, which is the volume distribution. Using a gamma DSD,

$$N(D) = N_0 D^\mu \exp(-\Lambda D), \quad (8)$$

the fractional volume of water can be written as,

$$f_w = \int_0^\infty \frac{4\pi}{3} \left(\frac{D}{2}\right)^3 N_0 D^\mu \exp(-\Lambda D) dD, \quad (9)$$

where μ , Λ , and N_0 are DSD parameters. Using the polarizability and the fractional volume of water, the refractive index of the air/water mixture is

$$n_{mix} = \sqrt{\left| \epsilon_{air} \frac{1 + 2f_w y}{1 - f_w y} \right|}, \quad (10)$$

which shows that no refractive index (hence, no refractivity) bias will occur in regions without precipitation because the fractional volume of water is zero.

Using (10), the refractivity biases was computed for a Marshall-Palmer DSD ($N(D) = 8000 \exp(-\Lambda D)$, special case of gamma DSD) for rainfall rates between 1 and 100 mm hr⁻¹ (Fig. 8). The precipitation bias ranged from 1 to 6.2 N-units for light to heavy rainfall rates. A 6.2 N-unit bias is approximately equal to a 1.2°C bias in dewpoint temperature at 20°C. Thus, the bias in absolute refractivity is relatively

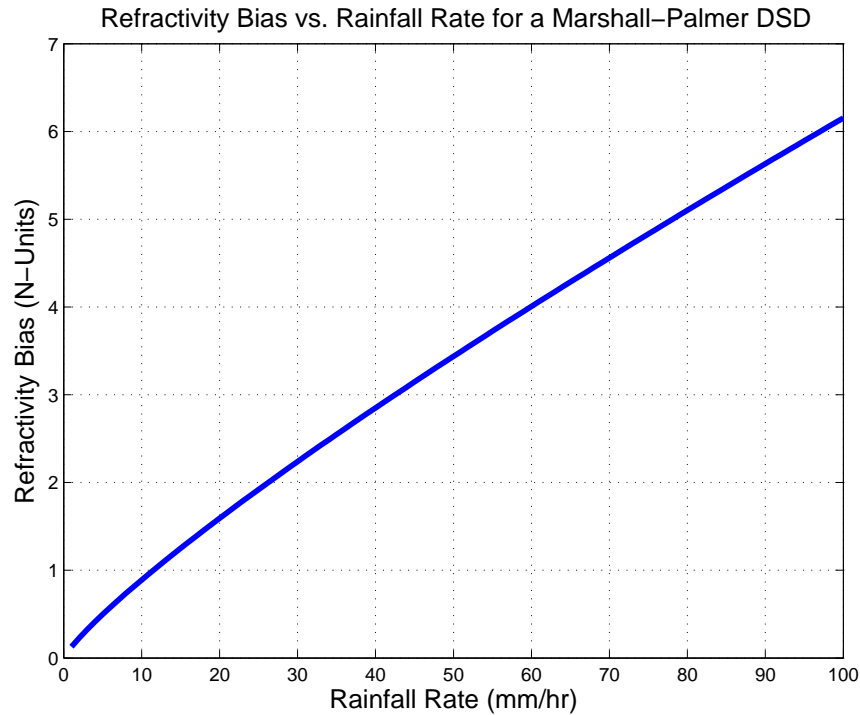


Figure 8: Plot of the refractivity bias caused by rainfall rates between 1 and 100 mm hr^{-1} , assuming a Marshall-Palmer DSD. The precipitation bias can exceed 6 N-units for rainfall rates near 100 mm hr^{-1} .

small, even at very heavy rainfall rates. However, scan-to-scan refractivity changes are typically on the order of 1 to 5 N-units. Thus, large errors in scan-to-scan refractivity could result from precipitation, even at light rainfall rates.

At heavier rainfall rates, observations of the precipitation bias may not occur because the QI sensors affected range gates. Fig. 1 shows an example of the censoring in refractivity and scan-to-scan refractivity. For this case, a positive bias is not prominent in the refractivity (Fig. 1a), or scan-to-scan refractivity data (Fig. 1b). The areas of missing refractivity data correspond to locations with heavy precipitation (Fig. 1d). The impact of the bias on the scan-to-scan refractivity field is not quite as intuitive. A negative bias in scan-to-scan refractivity would be observed in a region with a decreasing rainfall rate between scans, because the refractive index is decreasing. Hence, the variations in rainfall rate over the domain lead to a noisy scan-to-scan refractivity field.

Although the precipitation bias may already be mitigated by the clutter target censoring method, some precipitation bias could result in uncensored regions with lower rainfall rates. Furthermore, if more ground clutter targets in regions with precipitation can be obtained by filtering the in-phase and quadrature signal, refractivity data may be obtained in

regions with heavy precipitation. Hence, a greater need would exist for removing the precipitation bias.

A bias removal procedure could be developed, and would require a hydrometeor classification algorithm to determine areas of rainfall, and an algorithm to obtain the drop-size distribution to estimate the fractional volume of water. Straka et al. (2000) and Ryzhkov et al. (2005) established that fuzzy logic algorithms for hydrometeor classification can identify regions of rainfall, and other hydrometeor types using dual-polarimetric radar. Several studies (e.g., Brandes et al., 2004a,b; Cao et al., 2008) have obtained empirical relations between the polarimetric radar variables and drop-size distribution parameters, which could be used to produce estimates of the drop-size distribution. The theory relating the drop-size distribution to the refractive index and phase could be utilized to design an algorithm to correct the phase difference field. The refractivity algorithm applies significant smoothing to the phase difference field that smears the effects of the precipitation errors, thus phase difference errors would need to be corrected before the smoothing occurs.

4. SUPERCELL CASES

This section presents two cases illustrating refractivity applications for supercells and tornadogenesis. The 8 April 2008 case showed the capability to observe outflow from the rear-flank downdraft (RFD). Refractivity data resolved moisture differences between the RFD and the environment for the 2 May 2008 case. VCP 12 was operating during both cases, providing approximately 5-min refractivity measurements. For the 2 May 2008 case, one volume scan was missing at 0020 UTC, and two volume scans were missing between 0028 and 0041 UTC.

4.1. 8 April 2008

The 8 April 2008 supercell case showed that refractivity data could be used to identify the moisture characteristics within the gust front produced by the RFD. While this supercell passed through the refractivity domain, it had a well-defined hook echo in reflectivity (Fig. 9a). A gust front produced by the RFD was evident in reflectivity as a fine line extending southward from the hook echo and in radial velocity as convergent flow normal to the boundary.

As this gust front passed over the Oklahoma City North (OKCN) Mesonet station (between 0415 and 0425 UTC), the OKCN station measured an increase in dewpoint temperature of 0.5°C and a refractivity change from 321 to 323 N-units. The scan-to-scan refractivity change at 0428 UTC showed an increase in refractivity between 1 and 3 N-units behind the gust front, with the greatest positive scan-to-scan refractivity changes near the hook echo (Fig. 9b). Scan-to-scan changes of 1 to 3 N-units were also observed behind the gust front as it moved southeastward at 0445, 0502, and 0510 UTC (Fig. 9b). This case illustrated the utility of refractivity data in tracking the position of the gust front in addition to assessing moisture changes caused by the gust front.

4.2. 2 May 2008

The 2 May 2008 case demonstrated potential for refractivity applications for tornadogenesis forecasting. Refractivity data from the 2 May 2008 case showed near-surface moisture changes within the RFD and the updraft prior to a brief tornado. As the supercell developed, negative scan-to-scan refractivity changes were observed beneath the updraft of the supercell (not shown). The author observed a funnel cloud at 0013 UTC, approximately the same time as the first hook echo was observed in reflectivity on KTLX (Fig. 10a). While the storm was in the refractivity domain, negative scan-to-scan refractivity changes were observed within and east of the hook echo and positive scan-to-scan refractivity changes were observed to the northwest of

the hook echo, forming a couplet of positive and negative refractivity changes. Between 0015 and 0029 UTC, the couplet signature moved with the hook echo as the hook echo became more cyclonically curved (Fig. 10b). A very brief tornado was reported approximately 1 km northwest of Choctaw, Oklahoma at 0029 UTC, although this report has been disputed by many observers. By 0040 UTC, the hook echo was no longer observed in reflectivity and the supercell had occluded. A volume scan was missing from the data set between 0028 and 0040 UTC, so the occlusion of the RFD was not observed in radar refractivity.

Given the potentially large temperature and pressure perturbations within supercells and the small magnitude of scan-to-scan refractivity changes observed in these cases, temperature or pressure terms contribute more to refractivity changes. While the pressure contribution would require a 30-hPa change for a 1 N-unit change in refractivity, a 1°C change in temperature could cause a 1 N-unit change in refractivity. The dewpoint temperature was approximately 20°C. Thus, the change in refractivity required for a 1-K increase in dewpoint temperature is six times greater than the change required for a 1-K increase in temperature. Given the sensitivity of refractivity changes to moisture, the observed refractivity changes are most likely caused by moisture changes, but temperature changes cannot be ruled out. Another potential issue is the relatively sparse data coverage near the edge of the domain, as refractivity measurements near the edge of the domain are often noisy. However, the temporal continuity of the couplet and movement with the storm suggests that this signature is not caused by poor data.

5. SUMMARY AND DISCUSSION

The 8 April 2008 case illustrated the capability of radar refractivity retrievals to observe outflow associated with the RFD of a nontornadic supercell. The role of low-level outflow dissipating the mesocyclone and tornado is well-documented. A three-dimensional modeling study by Brooks et al. (1993) showed that cold outflow can cutoff the updraft and limit the duration of a mesocyclone. Dowell and Bluestein (1997) showed a case where low-level outflow moved ahead of the updraft, causing the dissipation of the tornado. Radar refractivity data could potentially identify low-level outflow that could cutoff the mesocyclone or tornado. For this case, a well-defined fine line was observed along the RFD gust front. However, in cases where a well-defined fine line or radial velocity signature is not observed, forecasters could use refractivity data to identify low-level outflow.

The capability to observe moisture changes within the RFD was demonstrated by the 2 May 2008 case. Moisture changes associated with the boundary between the RFD and the updraft were observed using radar refractivity

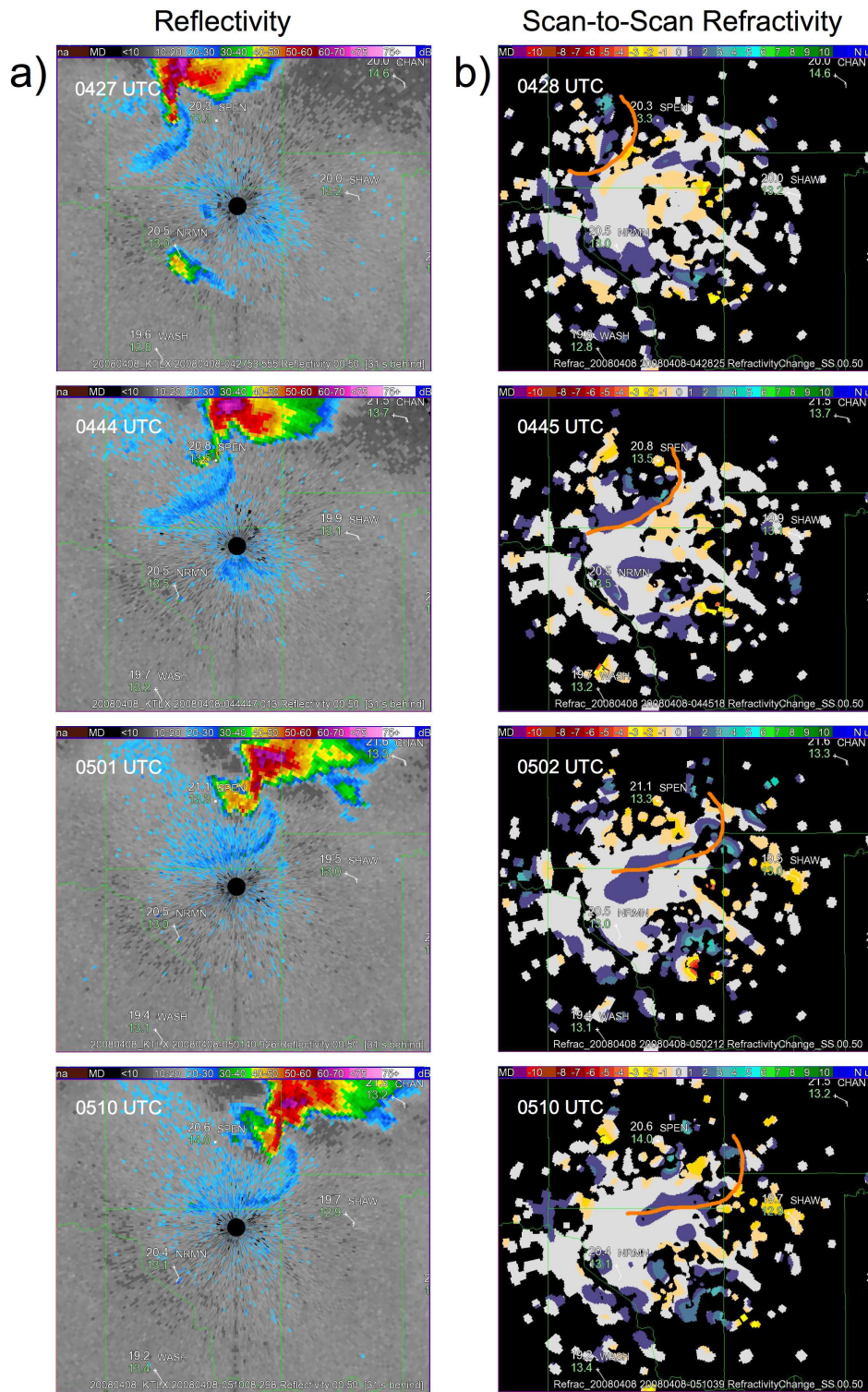


Figure 9: a) Scan-to-scan refractivity change, and b) 0.5°-tilt reflectivity at 0428, 0445, 0502, and 0510 UTC 8 April 2008. The orange line shows the position of the gust front in reflectivity.

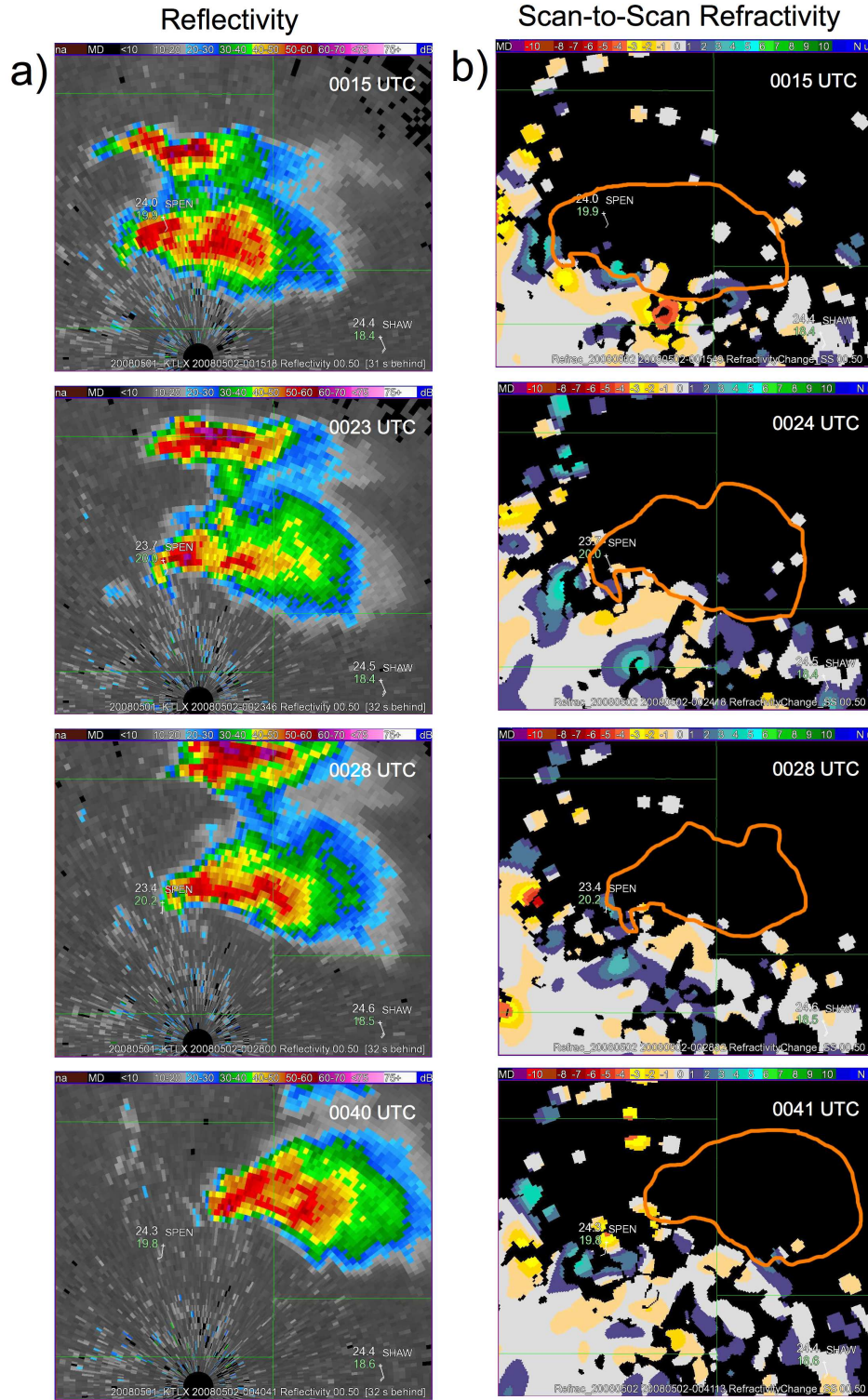


Figure 10: a) Scan-to-scan refractivity change, and b) 0.5°-tilt reflectivity at 0015, 0024, 0028, and 0041 UTC 2 May 2008. The orange line shows position of the storm indicated in reflectivity.

retrievals. The negative scan-to-scan refractivity changes suggest drying beneath the updraft. Previous studies showed that higher LCL heights decrease the likelihood of significant tornadoes, and lower boundary layer humidities decrease the likelihood of tornadogenesis. Thus, the drying beneath the updraft could partially explain the failure of tornadogenesis for this case. To determine what moisture fields could discriminate between tornadic and nontornadic supercells, output from numerical simulations or field observations could be used. Then, the moisture fields could be converted to refractivity to examine differences between tornadic and nontornadic supercells in refractivity data.

Although these cases show that the retrieval of moisture fields within supercells could be useful for tornadogenesis forecasts, two issues arise with refractivity retrievals in regions of precipitation. The first issue is that the component of backscattered phase from precipitation is random, so the variance of the phase measurements in precipitation will increase. Thus, noisier phase measurements will make accurate refractivity measurements more difficult. The second issue is a positive bias caused by precipitation, up to 6 N-units at heavy rainfall rates. Currently, most phase measurements within regions of heavy precipitation are censored because targets with radial velocity and spectrum width values above the radial velocity and spectrum width thresholds are censored. While increased variance and bias in regions of precipitation may not be observed in regions with heavy rainfall rates, the bias will be observed in uncensored regions of lighter precipitation.

Implementing a low-pass filter prior to computing the phase may improve phase measurements, and could provide more refractivity coverage in regions of precipitation. While filtering may address the increased variance in phase measurements by attenuating the precipitation signal, the precipitation bias issue still remains. A method for correcting the precipitation bias was outlined. Assuming the refractivity errors within precipitation regions are understood and mitigated, analysis of refractivity fields in supercells could improve tornadogenesis forecasts.

6. ACKNOWLEDGMENTS

Funding for this research was provided by the Radar Operations Center through grant number NA17RJ1227 and the National Science Foundation through grant number ATM0750790. The first author was supported by an American Meteorological Society Fellowship sponsored by the Raytheon Corporation. The authors thank the Radar Operations Center for maintaining the data flow from KTLX during the experiment.

References

- Bean, B. R., and E. J. Dutton, 1968: *Radio Meteorology*. Dover Publications, 435 pp.
- Bodine, D., P. L. Heinselman, B. L. Cheong, R. D. Palmer, and D. Michaud, 2008: Convection initiation and storm evolution forecasting using radar refractivity retrievals. in *24th Conf. on Severe Local Storms*.
- Bodine, D., P. L. Heinselman, B. L. Cheong, R. D. Palmer, and D. Michaud, 2009a: Radar refractivity applications for convective initiation forecasting and observations of the convective boundary layer. in *25th Conference on IIPS*, Phoenix, AZ.
- Bodine, D., P. L. Heinselman, R. D. Roberts, B. L. Cheong, and D. S. Michaud, 2009b: Survey of applications of radar refractivity retrievals. in *34th Conf. on Radar Meteorology*, Williamsburg, VA.
- Brandes, E. A., G. Zhang, and J. Vivekanandan, 2004a: Comparison of polarimetric radar drop size distribution retrieval algorithms. *J. Atmos. Oceanic Technol.*, **21**, 584–598.
- Brandes, E. A., G. Zhang, and J. Vivekanandan, 2004b: Drop size distribution retrieval with polarimetric radar: Model and application. *J. Appl. Meteorol.*, **43**, 461–475.
- Brock, F. V., K. C. Crawford, R. L. Elliott, G. W. Cuperus, S. J. Stadler, H. L. Johnson, and M. D. Eilts, 1995: The Oklahoma Mesonet: A technical overview. *J. Atmos. Oceanic Technol.*, **12**, 5–19.
- Brooks, H. E., C. A. Doswell, and R. B. Wilhelmson, 1993: The role of midtropospheric winds in the evolution and maintenance of low-level mesocyclones. *Mon. Wea. Rev.*, **122**, 126–136.
- Buban, M., C. Ziegler, E. Rasmussen, and Y. Richardson, 2007: The dryline on 22 May 2002 during IHOP: Ground-radar and in situ data analyses of the dryline and boundary layer evolution. *Mon. Wea. Rev.*, **135**, 2473–2505.
- Cao, Q., G. Zhang, E. Brandes, T. Schuur, A. Ryzkhov, and K. Ikeda, 2008: Analysis of video disdrometer and polarimetric radar data to characterize rain microphysics in Oklahoma. *J. Appl. Meteorol.*, **47**, 2238–2255.
- Cheong, B. L., R. D. Palmer, C. D. Curtis, T.-Y. Yu, D. S. Zrnić, and D. Forsyth, 2008: Refractivity retrieval using the Phased Array Radar: First results and potential for multi-function operation. *IEEE Tran. Geosci. Remote Sensi.*, **46**, 2527–2537.
- Demoz, B., C. Flamant, T. Weckwerth, D. Whiteman, K. Evans, F. Fabry, P. Girolamo, D. Miller, B. Geerts, W. Brown, G. Schwemmer, B. Gentry, W. Feltz, and Z. Wang, 2006: The dryline on 22 May 2002 during IHOP:

- Convective-scale measurements at the profiling site. *Mon. Wea. Rev.*, **134**, 294–310.
- Dowell, D. C., and H. B. Bluestein, 1997: The Arcadia, Oklahoma, Storm of 17 May 1981: Analysis of a supercell during tornadogenesis. *Mon. Wea. Rev.*, **125**, 2562–2582.
- Fabry, F., 2004: Meteorological value of ground target measurements by radar. *J. Atmos. Oceanic Technol.*, **21**(4), 560–573.
- Fabry, F., 2006: The spatial variability of moisture in the boundary layer and its effect on convective initiation: Project-long characterization. *Mon. Wea. Rev.*, **134**, 79–91.
- Fabry, F., C. Frush, I. Zawadzki, and A. Kilambi, 1997: On the extraction of near-surface index of refraction using radar phase measurements from ground targets. *J. Atmos. Oceanic Technol.*, **14**(4), 978–987.
- Heinselman, P. L., B. L. Cheong, R. D. Palmer, D. Bodine, and K. Hondl, 2009: Radar refractivity retrievals from KTLX: Insights into operational benefits and limitations. *Wea. Forecasting*, in press.
- Markowski, P. M., and Y. P. Richardson, 2009: Tornadogenesis: Our current understanding, forecasting considerations, and questions to guide future research. *Atmos. Research*, **93**, 3–10.
- Markowski, P. M., J. M. Straka, and E. N. Rasmussen, 2002: Direct surface thermodynamic observations within the rear-flank downdraft of nontornadic and tornadic supercells. *Mon. Wea. Rev.*, **130**, 1692–1721.
- Markowski, P. M., J. M. Straka, and E. N. Rasmussen, 2003: Tornadogenesis resulting from the transport of circulation by a downdraft: Idealized numerical simulations. *J. Atmos. Sci.*, **60**, 795–823.
- McLaughlin, D., D. Pepyne, V. Chandrasekar, B. Philips, J. Kurose, M. Zink, K. Droegemeier, S. Cruz-Pol, F. Junyent, J. Brotzge, D. Westbrook, N. Bharadwaj, Y. Wang, E. Lyons, K. Hondl, Y. Liu, E. Knapp, M. Xue, A. Hopf, K. Kloesel, A. DeFonzo, P. Kollias, K. Brewster, R. Contreras, T. Djaferis, E. Insanic, S. Frasier, and F. Carr, 2009: Short-wavelength technology and the potential for distributed networks of small radar systems. *Bull. Amer. Meteor. Sci.*, in press.
- McPherson, R. A., C. A. Fiebrich, K. C. Crawford, J. R. Kilby, D. L. Grimsley, J. E. Martinez, J. B. Basara, B. G. Illston, D. A. Morris, K. A. Kloesel, A. D. Melvin, H. Shrivastava, J. M. Wolfenbarger, J. P. Bostic, and D. B. Demko, 2007: Statewide monitoring of the mesoscale environment: A technical update on the Oklahoma Mesonet. *J. Atmos. Oceanic Technol.*, **24**, 301–321.
- Rasmussen, E. N., and D. O. Blanchard, 1998: A baseline climatology of sounding-derived supercells and tornado forecast parameters. *Wea. Forecasting*, **13**, 1148–1164.
- Roberts, R. D., F. Fabry, P. C. Kennedy, E. Nelson, J. Wilson, N. Rehak, J. Fritz, V. Chandrasekar, J. Braun, J. Sun, S. Ellis, S. Reising, T. Crum, L. Mooney, R. Palmer, T. Weckwerth, and S. Padmanabhan, 2008: REFRACTT-2006: Real-time retrieval of high-resolution low-level moisture fields from operational NEXRAD and research radars. *Bull. Amer. Meteor. Sci.*, **89**, 1535–1548.
- Ryzhkov, A. V., T. J. Schuur, D. W. Burgess, P. L. Heinselman, S. E. Giangrande, and D. S. Zrnić, 2005: The joint polarization experiment: Polarimetric rainfall measurements and hydrometeor classification. *Bull. Amer. Meteor. Sci.*, **86**, 809–824.
- Straka, J. M., D. S. Zrnić, and A. V. Ryzhkov, 2000: Bulk hydrometeor classification and quantification using polarimetric radar data: Synthesis of relations. *J. Appl. Meteorol.*, **39**, 1341–1372.
- Torres, S. M., and D. S. Zrnić, 1999: Ground clutter canceling with a regression filter. *J. Atmos. Oceanic Technol.*, **16**, 1364–1374.
- Wakimoto, R. M., and H. V. Murphey, 2008: Analysis of a dryline during IHOP: Implications for convection initiation. *Mon. Wea. Rev.*, **137**, 912–936.
- Weckwerth, T. M., C. R. Pettet, F. Fabry, S. Park, M. A. LeMone, and J. W. Wilson, 2005: Radar refractivity retrieval: Validation and application to short-term forecasting. *J. Appl. Meteorol.*, **44**(3), 285–300.
- Zrnić, D. S., J. F. Kimpel, D. E. Forsyth, A. Shapiro, G. Crain, R. Ferek, J. Heimmer, W. Benner, T. J. McNellis, and R. J. Vogt, 2007: Agile-beam phased array radar for weather observations. *Bull. Amer. Meteor. Sci.*, **88**, 1753–1766.